Regular Article

PHYSICAL CHEMISTRY RESEARCH
Published by the
Iranian Chemical Society
www.physchemres.org
info@physchemres.org

Phys. Chem. Res., Vol. 12, No. 3, 771-781, September 2024
DOI: 10.22036/pcr.2024.396888.2338

Structural, Optical, and Luminescent Studies of Vanadyl Doped Strontium Tin Phosphate by Solid-state Reaction Method

Y.V.K. Suresh[a], N. Chinna Anjaneyulu[a], A. Rajendrakumar[b], A.V. Chandarasekhar[c] and R.V.S.S.N. Ravikumar[a,*]

[a]*Department of Physics, Acharya Nagarjuna University, Nagarjuna Nagar, Guntur 522510, A.P, India*
[b]*Department of Physics and Electronics, Chaitanya Deemed to University, Hanamkonda 506001, T.S, India*
[c]*Department of Physics, S.V. Arts College, Tirupati 517502, A.P., India*
(Received 12 May 2023, Accepted 28 January 2024)

VO^{2+} doped $SrSn(PO_4)_2$ nanopowder was prepared by solid-state reaction method. The obtained nanopowder was studied using XRD, SEM, HR-TEM, FT-IR, optical absorption, EPR, and PL measurements. The X-ray diffraction analysis revealed a monoclinic structure of VO^{2+} doped $SrSn(PO_4)_2$ nanopowder and exhibited an average crystallite size of 26 nm. The size is in the nano scale and the W-H plot approach was also in agreement with this value. SEM and HR-TEM images show the non-uniform stone-like particle morphology of the prepared sample and confirm information about the average particle size of nanopowder, while EDS analysis confirms elemental composition. The selected area electron diffraction pattern revealed the sample crystalline by means of rings corresponding to XRD planes. Vibration modes related to phosphate functional groups were observed in FT-IR studies. The optical absorption spectrum shows characteristic VO^{2+} peaks at 520, 668, and 824 nm, and the crystal field and tetragonal parameters were evaluated: Dq = 1497, Ds = -2331, and Dt = 1028 cm^{-1}. From the EPR spectrum, Hamiltonian parameters and hyperfine coupling constant values were calculated. The associated CIE chromaticity coordinates and CCT parameters were computed from the PL spectrum, and they indicate possible applications in LEDs and lighting devices.

Keywords: $SrSn(PO_4)_2$, Solid state reaction method, XRD, FTIR, HR-TEM, EPR, PL

INTRODUCTION

In the earlier two eras, nanotechnology has fetched different changes from other technologies, several new revolutions are found in materials and monitored their structures, useful to several applications. Another significant part of nanotechnology is the miniaturization of present and new instruments, machines, and sensors. This will show an extraordinary effect on the world we reside in [1,2].

Due to their good homogeneity, high brightness, wide band gap and thermal stabilities at sintering temperature, phosphate-based compounds have received a lot of attention recently [3,4]. Numerous studies have shown that the dimensions, shape, and chemical composition of functional materials have an impact on their physical, chemical, and mechanical capabilities. One-dimensional nanomaterials, such as nanorods, nanowires, nanofibers, and nanotubes are frequently employed in the production of electrical, photocatalytic, optical, and luminescent devices [5-8]. In display devices and solid-state lightening Apatite-type phosphors play a crucial role [9,10].

Numerous techniques were used to prepare the phosphate-based nanophosphors [11]. Solid state reaction (SSR) is the best method for the creation of nanophosphors and to grow polycrystalline materials [12,13]. Rare earth (RE) metal ions exhibit high luminescence properties, and the synthesis of RE-doped materials requires a very high temperature. However, transition metal (TM) ions may be appropriate to replace the RE ions [14]. Strontium (Sr) is an alkaline earth metal useful in the formation of bone and it has other outstanding qualities, such as radio-opacity and antibacterial activity [15,16]. Tin phosphates are effectively

*Corresponding author. E-mail: rvssn@yahoo.co.in

used as sorbents, electrical probes, and reagents [17,18]. Due to their multidisciplinary nature, vanadium ions are used in the field of luminescence, sensors, lasers, and as a cathode in lithium-ion battery technologies. Vanadyl-doped materials exhibit sufficient catalytic nature for reversible redox cycles between V^{4+} and V^{5+} states. Vanadyl ions play a crucial function as a dopant in phosphate applications because of their long-wavelength excitation and emission capabilities [19]. In the present work, for the first time, an attempt is made to prepare the $SrSn(PO_4)_2$:VO^{2+} nanopowder by SSR method and consider its various structural, morphological, and optical properties as new LED material.

SYNTHESIS AND CHARACTERIZATION

Analytical grade chemicals, Strontium Chloride Hexahydrate ($SrCl_2.6H_2O$, 99.9%), Ammonium dihydrogen orthophosphate ($NH_4H_2PO_4$,99.9%), Stannous Chloride Pentahydrate ($SnCl_4.5H_2O$, 99.9%) and 0.01mol% of Vanadium pentoxide (V_2O_5) were procured from HiMedia Laboratories Pvt. Ltd, Mumbai, India were used as starting reagents for the fabrication of vanadyl doped $SrSn(PO_4)_2$ (STP) nanopowder.

In order to prepare the sample, 2.666 g of $SrCl_2.6H_2O$, 7.003 g of $NH_4H_2PO_4$, and 2.300 g of $SnCl_4.5H_2O$ were weighed according to stoichiometric proportions and ground for 30 min using an agate mortar and pestle. Then, the mixture was inserted into a crucible and subjected to high temperature using programmable muffle furnace. The synthesis was carried out at 500 °C for 2 h, and then, the crucible was taken out and cooled. Then, the sample was ground well. At the next step, the sample was treated at 950 °C for 2 h. The crude product was remained then allowed to cool or become evenly powdered at room temperature. The final powder substance was used for characterizations.

A PanAnalytical X-pert powder diffractometer CuKα (1.5406 Å), 2θ = 6º to 60º was used to record the PXRD pattern. SEM patterns with EDS were recorded by using a JEOL JSM-IT 500 for surface morphology and chemical composition. Micrographs, surface topography, and selected area electron diffraction (SAED) patterns were obtained using JEOL JEM-2100 High-Resolution Transmission Electron Microscopy (HR-TEM). A Shimadzu IRAffinity-1S FT-IR instrument was employed to capture spectrum over 400-4000 cm^{-1}. UV-VIS absorption spectrum in the range of 200-900 nm was recorded by a JASCO instrument. The EPR spectrum of the prepared powder was taken using a JEOL JES-TE 100 EPR spectrometer. A Horiba JY Fluorescence spectrometer fitted with a 450W Xenon lamp was used to measure the PL spectrum.

RESULTS AND DISCUSSION

X-ray Diffraction Studies

The diffraction pattern for the VO^{2+} doped sample exhibited several peaks, as shown in Fig. 1. This pattern is well matched with the reported JCPDS File no. 33-150 [20,21]. $SrSn(PO_4)_2$ has exhibited monoclinic system with C2/c space group. Sr^{2+} is bonded with 8-coordinate geometry around eight O^{2-} atoms. Sr–O bond distances ranging from 2.61-2.99 Å. Sn^{4+} is bonded to six O^{2-} atoms to form SnO_6 octahedra that share corners with six equivalent PO_4 tetrahedra. The lattice parameters reported as a = 1.689, b = 0.531, c = 0.816 nm, β = 115.43º. The Debye-Scherrer's formula was used to determine the crystallite size of the VO^{2+} doped $SrSn(PO_4)_2$ sample [14].

$$D = \frac{0.9\,\lambda}{\beta\,\cos\theta} \quad (1)$$

By using K = 0.9 (shape factor), $\lambda = 1.5406$ Å (X-ray wavelength), FWHM of the most intense diffraction line (β) and Diffraction angle (θ) the estimated crystallite size is 26 nm. By the W-H plot method average crystallite size is determined as 33 nm and the related plot is shown in Fig. 2.

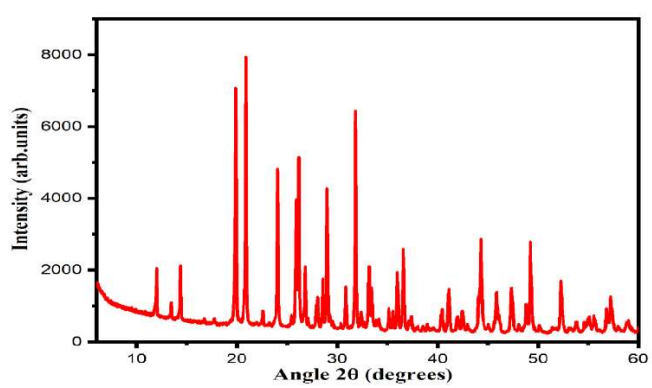

Fig. 1. XRD pattern of VO^{2+} doped $SrSn(PO_4)_2$ nanopowder.

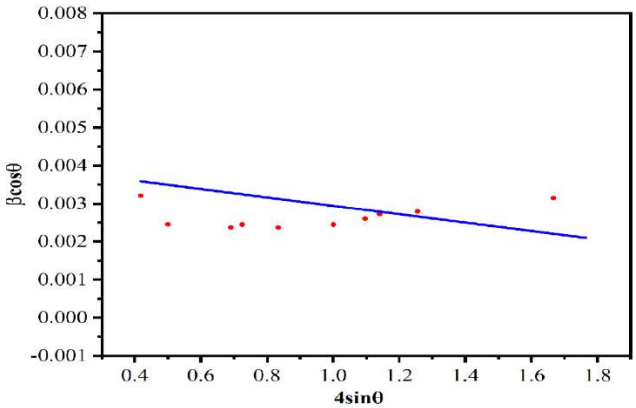

Fig. 2. W-H plot of VO^{2+} doped $SrSn(PO_4)_2$ nanopowder.

The cell parameters of VO^{2+} doped $SrSn(PO_4)_2$ nanopowder are determined as a = 1.665 nm, b = 0.526 nm, c = 0.798 nm, and $\beta = 115.69^{\circ}$. The small variations in the lattice cell parameters may be due to VO^{2+} impurity entering into the lattice. The calculated and observed values of Miller indices and d-spacings are tabulated in Table 1. The micro-strain (ε) and dislocation density (δ) of preparing STP: VO^{2+} sample was also calculated using relation equations $\varepsilon = \frac{\beta \cos\theta}{4}$ and $\delta = \frac{1}{D^2}$ as 0.1303×10^{-3} and $1.479 \times 10^{15} \frac{lines}{m^2}$ respectively as shown in Table 2.

Table 1. Miller Indices of Vanadyl Doped Strontium Tin Phosphate with ±0.001 Error

2θ		d-spacing		Relative			
Observed	Calculated	Observed	Calculated	Intensity	h	k	l
11.991	11.926	7.419	7.528	12	2	2	0
17.718	16.776	5.002	5.281	03	1	1	0
20.849	19.377	4.257	4.577	100	1	1	-1
22.501	22.434	3.995	3.960	04	1	1	1
26.031	26.324	3.420	3.383	44	4	0	-2
27.973	28.108	3.187	3.172	15	1	1	-2
28.976	28.667	3.079	3.111	51	3	1	-2
30.829	30.394	2.898	2.939	16	3	1	1
31.793	31.429	2.812	2.844	78	5	1	-1
34.164	34.666	2.622	2.823	04	0	2	0
35.925	36.120	2.498	2.485	23	6	0	0
36.562	34.156	2.456	2.623	38	0	2	1
37.316	38.005	2.408	2.366	07	3	1	-3
39.509	38.083	2.279	2.361	01	2	2	1
40.384	40.253	2.239	2.239	12	3	1	2
41.080	39.338	2.195	2.289	23	2	2	-2
45.895	47.381	1.975	1.917	15	2	0	-4
47.341	45.791	1.919	1.980	25	2	2	2
49.229	48.128	1.849	1.889	44	4	2	-3
50.123	50.230	1.819	1.815	04	5	1	2
51.444	51.930	1.775	1.759	02	3	1	3
52.272	52.611	1.749	1.738	37	9	1	-2
53.766	51.204	1.704	1.782	06	1	3	1
55.668	51.905	1.650	1.760	06	3	3	0
57.137	55.809	1.611	1.646	09	8	2	-1

Table 2. XRD Parameters for Vanadyl Doped Strontium Tin Phosphate

Sample name	Scherrer's method			W-H method		
	D (nm)	$\delta \times 10^{15}$	$\varepsilon \times 10^{-3}$	D (nm)	$\delta \times 10^{15}$	$\epsilon \times 10^{-3}$
VO^{2+} doped	26	1.479	0.1305	33	9.182	-0.11

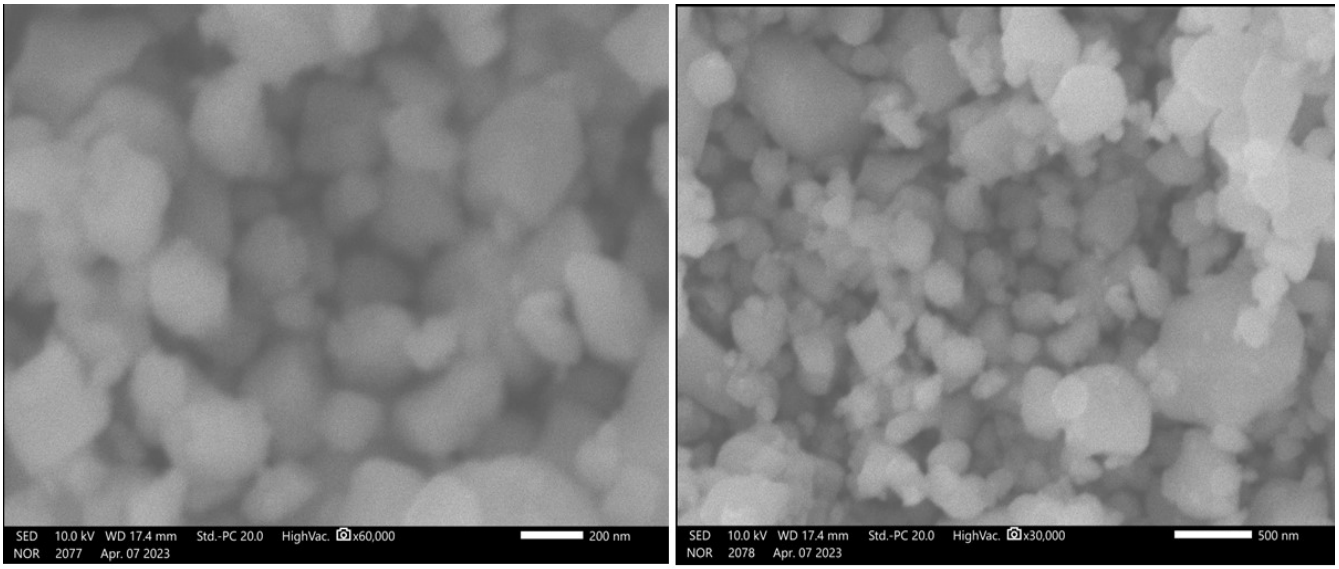

Fig. 3. SEM images of VO^{2+} doped $SrSn(PO_4)_2$ nanopowder.

Morphological Studies

SEM is commonly used to observe the surface morphology of prepared sample. Figure 3 depicts SEM images of VO^{2+} doped $SrSn(PO_4)_2$ nanopowder. The SEM images exhibited non-uniformly distributed stone-like structures with characteristic size below 37 nm [22]. The histogram graph of the particle size distribution is represented in Fig. 4. EDS spectrum of VO^{2+} doped $SrSn(PO_4)_2$ nanopowder is represents in Fig. 5 and it displays the presence of independent peaks of Strontium (Sr), Oxygen (O), Tin (Sn), Phosphorous (P), and Vanadium (V) species.

HR-TEM Analysis

HR-TEM images and SAED patterns can provide phase structure and morphology studies for synthesized sample. Fig. 6a shows the HR-TEM image of VO^{2+} doped $SrSn(PO_4)_2$ nanopowder with magnification of 100 nm. HR-TEM images of the sample clearly demonstrated stone-like structures.

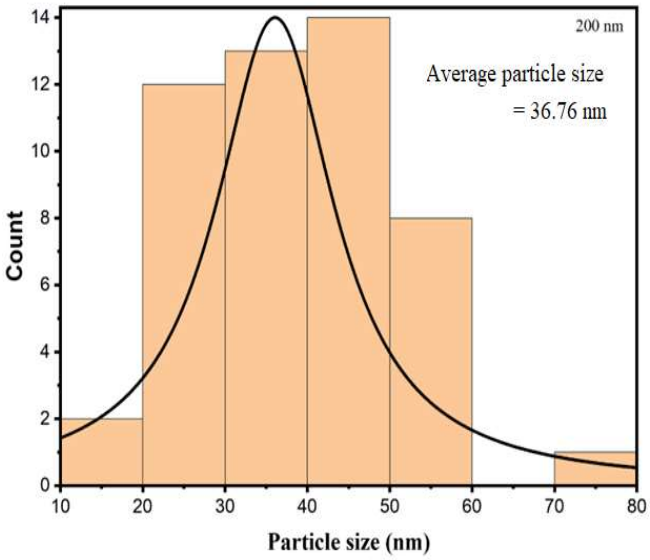

Fig. 4. SEM Histogram graph of VO^{2+} doped $SrSn(PO_4)_2$ nanopowder.

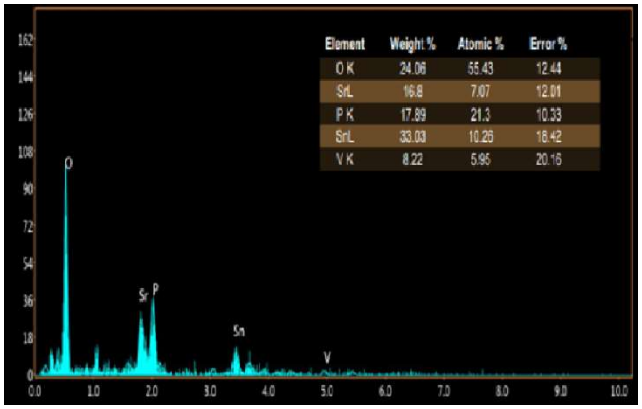

Fig. 5. EDS pattern of VO^{2+} doped $SrSn(PO_4)_2$ nanopowder.

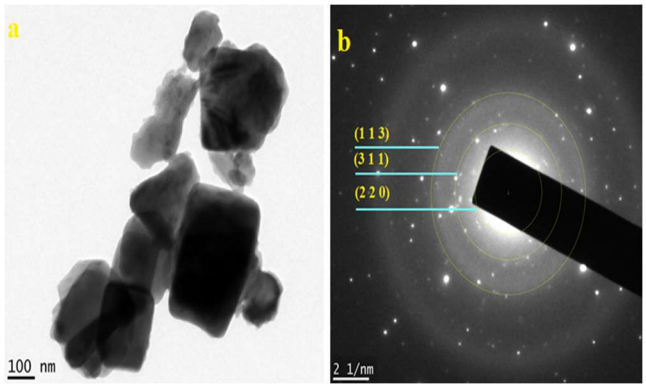

Fig. 6. (a) HR-TEM micrographs (b) SAED pattern of VO^{2+} doped $SrSn(PO_4)_2$ nanopowder.

Figure 6b exhibited the selected area electron diffraction (SAED) pattern of the sample. The ring patterns of (2 2 0), (3 1 1), and (1 1 3) shown in Fig. 6b confirm the particles are crystalline in nature and matched with XRD analysis. Figure 7 gives the average particle size observed using TEM image of 100 nm by histogram analysis was said to be around 30 nm with the help of image-J software.

FT-IR Analysis

Figure 8 is the vibration spectrum of VO^{2+} doped $SrSn(PO_4)_2$ nanopowder. The spectrum shows the typical symmetric, asymmetric bending, and stretching vibrations of phosphate and hydroxyl ions. The phosphate ion has four fundamental frequencies and tetrahedral (T_d) symmetry. $SrSn(PO_4)_2$ sample exhibits P-O-H vibration modes between

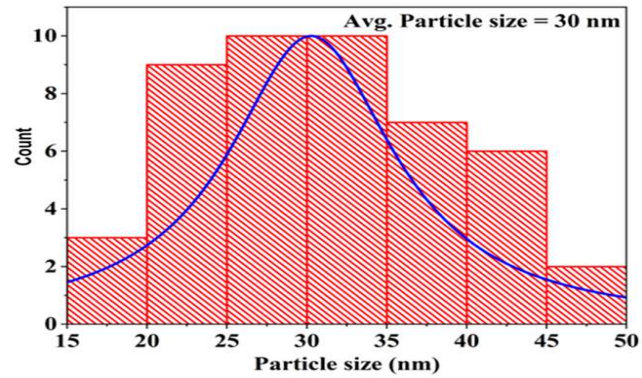

Fig. 7. HR-TEM Histogram graph of VO^{2+} doped $SrSn(PO_4)_2$ nanopowder.

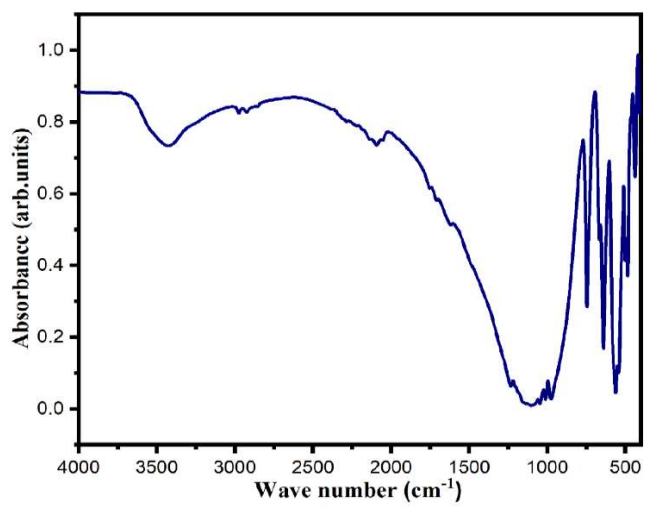

Fig. 8. FTIR spectrum of VO^{2+} doped $SrSn(PO_4)_2$ nanopowder.

1500 and 2400 cm^{-1} [23,24]. The band observed at 997 cm^{-1} is assigned to $(PO_4)^{3-}$ ion as (ν_1) symmetric stretching mode. Symmetric (ν_2) and asymmetric (ν_4) bending vibrations were identified at 438 cm^{-1} and 501, 541, 667 cm^{-1}, while asymmetric stretching vibrations (ν_3) occurred at 1009, 1044 and 1234 cm^{-1}. The bending modes (ν_2) hydroxyl group were represented by the vibrational bands at 1593, 1701, and 1753 cm^{-1}, whereas the P-O-H mode of vibration was represented by the bands at 2072, 2270, and 2367 cm^{-1} [14,25-27]. In Table 3 all vibrational bands and their assignments are shown.

Table 3. Vibrational Band Head Data and their Assignments of VO^{2+} Doped $SrSn(PO_4)_2$ Nanopowder

Vibrational frequency (cm^{-1})	Band assignment
438	Symmetric bending mode of PO_4^{3-} (ν_2)
511, 550, 659	Asymmetric bending mode of PO_4^{3-}(ν_4)
770	Symmetric stretching mode of P-O-P band
997	Symmetric stretching mode of PO_4^{3-} ($\nu_{1)}$
1026, 1061, 1217	Asymmetric bending mode of PO_4^{3-} (ν_3)
1593, 1701, 1753	Bending modes of hydroxyl ions
2072, 2947, 3654	Vibrational modes of P-O-H band

Optical Absorption Studies

Typically, a vanadium compound consists of 5 or 6 oxygen atoms where one of the oxygen atoms forms a vanadyl ion through a double covalent bond with the metal. Ground state $^2T_{2g}$ is produced when unpaired d^1 electron occupies the t_{2g} solitary unpaired electron of VO^{2+} ions. When the electron transits to the upper orbital e_g and ^2E_g creates the term by absorbing the energy. In reality, $^2T_{2g} \rightarrow {}^2E_g$ changes to a perfect octahedral symmetry for the electron. To witness the John-Teller effect, VO^{2+} must migrate to a reduced tetragonal symmetry (C_{4v}) as it never exhibits pure octahedral symmetry. The $^2T_{2g}$ term, which breaks into the $^2B_{2g}$ and ^2E_g sublevels, is a singlet in the ground state. The state ^2E_gthen is divided into the states $^2B_{1g}$ and $^2A_{1g}$. Three different transitions are possible, *i.e.* $^2B_{2g} \rightarrow {}^2E_g$, $^2B_{2g} \rightarrow {}^2B_{1g}$, and $^2B_{2g} \rightarrow {}^2A_{1g}$. The order of energy level is $^2B_{2g} < {}^2E_g < {}^2B_{1g} < {}^2A_{1g}$ [11]. Figure 9 shows the UV-visible absorption spectrum of VO^{2+} doped strontium tin phosphate nanopowder. We identified three bands in this spectrum at 572, 668, and 824 nm as shown in Fig. 9.

$$^2B_{2g} \rightarrow {}^2E_g\left(d_{xy} \rightarrow d_{xz,yz}\right) \quad (2)$$

$$^2B_{2g} \rightarrow {}^2B_{1g}\left(d_{xy} \rightarrow d_{x^2-y^2}\right) \quad (3)$$

$$^2B_{2g} \rightarrow {}^2A_{1g}\left(d_{xy} \rightarrow d_{z^2}\right) \quad (4)$$

The following equations can be used to compute the tetragonal field parameters (Ds) and (Dt), as well as the crystal field parameter (Dq).

$$^2B_{2g} \rightarrow {}^2E_g = -3Ds + 5Dt = 12133\ cm^{-1} \quad (5)$$

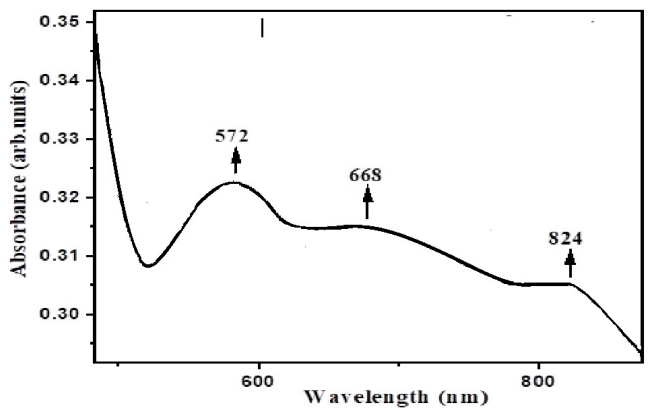

Fig. 9. Absorption spectrum of VO^{2+} doped $SrSn(PO_4)_2$ nanopowder

$$^2B_{2g} \rightarrow {}^2B_{1g} = 10Dq = 14965\ cm^{-1} \quad (6)$$

$$^2B_{2g} \rightarrow {}^2A_{1g} = 10Dq - 4Ds - 5Dt = 19151\ cm^{-1} \quad (7)$$

and obtained values are Dq = 1497, Ds = -2331, and Dt = 1028 cm^{-1}. The calculated values are in good agreement with earlier reports [28]. The band gap analysis was implemented by using the reflectance data, and the Kubelka-Munk absorption function (K/S) was plotted by the following equation [29]:

$$F(R) = (1-R)^2/2R = K/S \quad (8)$$

From Fig. 10 the band gap of STP: VO^{2+} was estimated as equal to 2.88 eV. The band gap value offers a potential for use in devices like LEDs and photovoltaic cells.

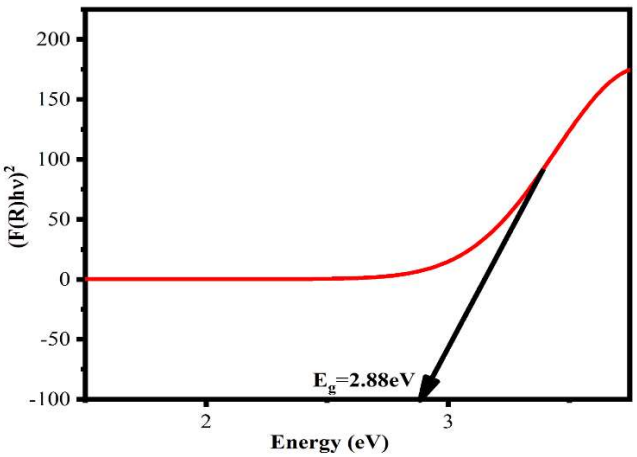

Fig. 10. Energy bandgap of VO^{2+} doped $SrSn(PO_4)_2$ nanopowder.

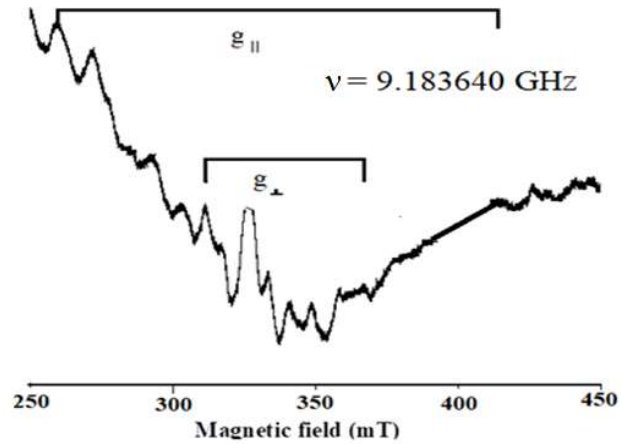

Fig. 11. EPR spectrum of VO^{2+} doped $SrSn(PO_4)_2$ nanopowder.

EPR Studies

EPR is a potent method for describing the bonding nature with the ligands. Paramagnetic ions and their symmetry with ligands can also be determined from the EPR spectrum. At low concentration of paramagnetic ion, electronic (S = 1/2) and Zeeman interactions (I = 7/2) with selection rules, spectrum exhibits hyperfine octet structure. The isolated V^{4+} ions are shown by the resonance signal's sharper lines. As recorded at room temperature, the EPR spectrum of the sample is presented in Fig. 11 and it shows the resonance signals. The calculated values of $g_\parallel = 1.9323$, $g_\perp = 1.9712$, $A_\parallel = 207 \times 10^{-4}$ and $A_\perp = 56 \times 10^{-4}$ cm^{-1} respectively. If the VO^{2+} doped sample exhibits $g_\parallel < g_\perp < g_e$ and $A_\parallel > A_\perp$ gives the tetragonally distorted octahedral symmetry [30]. The tetragonality of the vanadyl compound was evaluated by $\Delta_\parallel/\Delta_\perp = (g_e - g_\parallel)/(g_e - g_\perp) = 1.2335$. If this ratio is greater than one, the VO^{2+} ions tetragonally deformed character will be seen in the host lattice.

By using optical and EPR data, we calculate molecular bonding coefficients β_1^2, β_2^2. The following equations [31] give the Fermi contact term (κ) and dipolar coupling constant (P).

$$g_\parallel = g_e[1 - \left(\frac{4\lambda\beta_1^2\beta_2^2}{\Delta_\parallel}\right)] \quad (9)$$

$$g_\perp = g_e[1 - \left(\frac{4\lambda\gamma^2\beta_2^2}{\Delta_\perp}\right)] \quad (10)$$

Here $g_e = 2.0023$ is the free electron, λ (= 170 cm^{-1}) is spin orbit coupling constant, β_1 and β_2 were the degree of in-plane σ and π bonding respectively.

$$A_\parallel = P[-\frac{4}{7}\beta_2^2 - \kappa + (g_\parallel - g_e) + \frac{3}{7}(g_\perp - g_e)] \quad (11)$$

$$A_\perp = P[\frac{2}{7}\beta_2^2 - \kappa + \frac{11}{14}(g_\perp - g_e)] \quad (12)$$

Where, $A_\parallel$ and $A_\perp$ are parallel and perpendicular components of hyperfine coupling. The value of dipolar constant (P) = -165 × 10^{-4} cm^{-1} is calculated from the following equation while ignoring second-order effects,

$$P = \frac{7(A_\parallel - A_\perp)}{6 + \frac{3}{2}(\frac{\lambda}{\Delta_\perp})} \quad (13)$$

The isotropic values of g and A are determined by the following equations

$$g_{iso} = \frac{2(g_\perp + g_\parallel)}{3} \quad (14)$$

$$A_{iso} = \frac{2(A_\perp + A_\parallel)}{3} \quad (15)$$

Using Eqs. (14) and (15) Fermi constant can be evaluated as

$$\kappa = -\frac{A_{iso}}{P} - (g_e - g_{iso}) \quad (16)$$

The obtained κ = 0.728 value indicates a weak contribution from the vanadium 4s orbital to the vanadyl bond in the produced sample, while the values β_1^1 = 0.770, β_2^2 = 1.109 and γ^2 = 0.998 are evaluated these values are in the range of 0.5 and 1.0, respectively, suggesting the existence of partial covalent bonding in planar bonds.

Theoretical Studies of Optical and EPR Parameters

The total single electron wave function including the contributions from p- and s-orbitals of ligands may be expressed as

$$\Psi_t = N_t^{1/2} (\phi_t - \lambda_t\chi_{pt}) \quad (17)$$

$$\Psi_e = N_e^{1/2} (\phi_e - \lambda_e\chi_{pe} - \lambda_s\chi_s) \quad (18)$$

Were ϕ_γ (the subscript γ = e of t stands for the irreducible representation of O_h group) is d-orbital of $3d^n$ ion. $\chi_{p\gamma}$ and χ_s are p-orbital and s-orbital of ligand. N_γ and λ_γ (or λ_s) are respectively, normalization factors and orbital mixing coefficients. The normalization relationship can be given as

$$N_t (1 - 2\lambda_t S_{dpt} + \lambda_t^2) = 1 \quad (19)$$

$$N_e (1 - 2\lambda_e S_{dpe} - 2\lambda_s S_{ds} + \lambda_e^2 + \lambda_s^2) = 1 \quad (20)$$

And the approximate relationships

$$N^2 = N_t^2 [1 + 2\lambda_t^2 S_{dpt}^2 - 2\lambda_t S_{dpt}] \quad (21)$$

$$N^2 = N_e^2 [1 + \lambda_e^2 S_{dpe}^2 + \lambda_s^2 S_{ds}^2 - 2\lambda_e S_{dpe} - 2\lambda_s S_{ds}] \quad (22)$$

Here N is the average covalency factor characteristic of the covalency effect (or reduction of spin-orbit coupling coefficient and dipolar hyperfine structure parameter) of the central ion in crystals. The spin-orbit coupling coefficients and orbital reduction factors can be written as

$$\xi = N_t (\xi_d + \lambda_t\xi_p/2) \quad (23)$$

$$\acute{\xi} = (N_t N_e)^{1/2} (\xi_d - \lambda_t\lambda_e\xi_p/2) \quad (24)$$

$$k = N_t (1 + \lambda_t^2/2) \quad (25)$$

$$\acute{k} = (N_t N_e)^{1/2} [1 - \lambda_t(\lambda_e + \lambda_s A)/2] \quad (26)$$

where ξ_d and ξ_p are the spin-orbit coupling coefficients of $3d^n$ and ligand ion in free states respectively. A denotes the integral $R \langle ns \left|\frac{\partial}{\partial y}\right| np_y \rangle$, where R ≈ 0.195 nm is the impurity ligand distance in the studied system. For the free V^{4+} and O^{2-} ions, we have ξ_d ≈ 248 cm^{-1}, P ≈ 136 × 10^{-4} cm^{-1} for V^{4+} and ξ_p ≈ 151 cm^{-1} for O^{2-} respectively. Here λ_t, λ_e, N_t, N_e, S_{dpt}, and S_{dpe} are taken from reference [32] and the spin-orbit coupling coefficients (ξ, $\acute{\xi}$), normalization factor (N_γ) and orbital mixing coefficients (λ_γ, λ_s) can be obtained as shown in Table 4.

By using the perturbation procedure g factors for a $3d^1$ ion under octahedral tetragonal symmetry can be obtained from the cluster approach

$$g_\parallel = g_e - 8\frac{k'\xi'}{E_1} - \frac{2k\xi^2}{E_2^2} + \frac{2k'\xi'^2}{E_1^2} \quad (27)$$

$$g_\perp = g_e - 2\frac{k\xi}{E_2} - 2k'\xi'\xi\left[\frac{1}{E_1E_2} - \frac{1}{E_1^2}\right] \quad (28)$$

The energy denominators E_1 and E_2 stand for the energy separation between the excited $^2B_1$, ^2E, and the ground $^2B_2$ states. They can be expressed in terms of tetragonal field parameters Ds, Dt, and cubic field parameter Dq optical spectrum band positions are calculated. The theoretical and experimental optical and EPR parameters $g_\parallel$, $g_\perp$ $A_\parallel$, $A_\perp$, β_1^2, β_2^2, γ^2 and P are calculated and also shown in Table 5 which are well agreed.

Photoluminescence Study

The emission spectrum of VO^{2+} doped STP nanopowder in the region of 350-600 cm^{-1} is shown in Fig. 12. The visible part of the spectrum displays many bands, with the band at 411 nm in blue region and the band at 496 nm in green color

Table 4. Spin-orbit Coupling Coefficients (ξ and $\acute{\xi}$ in cm^{-1}) and Orbital Reduction Factors (k and $\acute{k}$) of VO^{2+} Doped $SrSn(PO_4)_2$ Nanopowder

ξ	$\acute{\xi}$	k	$\acute{k}$	N^2
233.98	221.65	0.969	0.819	0.785

zone. Observed bands could be the result of structural flaws such as point defects or surface conurbations, among other things. The blue band could be the result of radiation electron recombination that occurred from a local flaw by holes in the top of the valance band [31]. The McCamy equation is used to calculate the CCT value.

Table 5. Optical Spectrum Band Positions (cm^{-1}) and EPR Parameters of VO^{2+} Doped $SrSn(PO_4)_2$ Nanopowder

	Experimental	Theoretical
$^2B_{2g} \rightarrow {}^2E_g$	12133	12133
$^2B_{2g} \rightarrow {}^2B_{1g}$	14965	14965
$^2B_{2g} \rightarrow {}^2A_{1g}$	19151	19151
$g_{\parallel}$	1.9323	1.9203
$g_{\perp}$	1.9712	1.9649
$A_{\parallel}$ (10^{-4} cm^{-1})	207	246
$A_{\perp}$ (10^{-4} cm^{-1})	56	69
β_1^2	0.7703	0.9023
β_2^2	1.1098	1.3343
γ^2	0.998	0.993
P (10^{-4} cm^{-1})	165	134

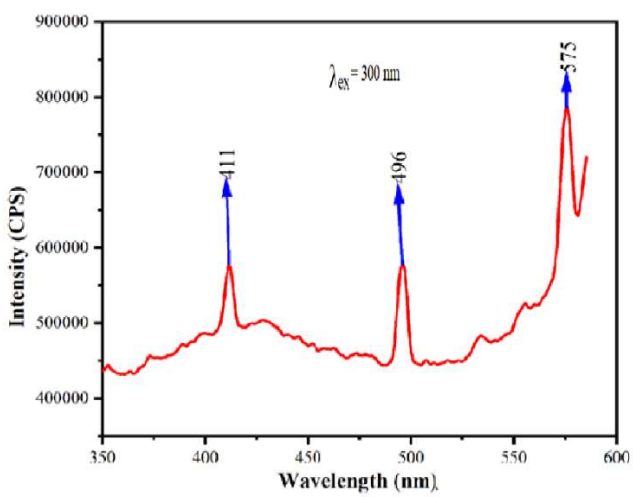

Fig. 12. Photoluminescence spectrum of VO^{2+} doped $SrSn(PO_4)_2$ nanopowder.

$$CCT = -437n^3 + 3601n^2 - 6861n + 5514.31 \quad (29)$$

The chromaticity epicenter in this instance is located at (0.3320, 0.1858), and the CCT value is 11637 K, as shown in Fig. 13. The created sample emits a mild blue color and it may be interesting in display screens and other LED devices.

CONCLUSION

VO^{2+} doped $SrSn(PO_4)_2$ nanopowder was prepared successfully through the solid-state reaction method. From XRD studies, the prepared nanopowder was attributed to monoclinic crystal system, and the average crystallite size was 26 and 33 nm from Debye-Scherrer's and W-H methods, respectively. The SEM and HR-TEM images showed the irregular stone-like particle morphology and the average particle size was determined in order of nano size. From EDS results the presence and amount of chemicals were obtained. The SAED ring patterns indicate that the particles are crystalline in nature. Each ring corresponds to the different lattice planes obtained from the XRD analysis.

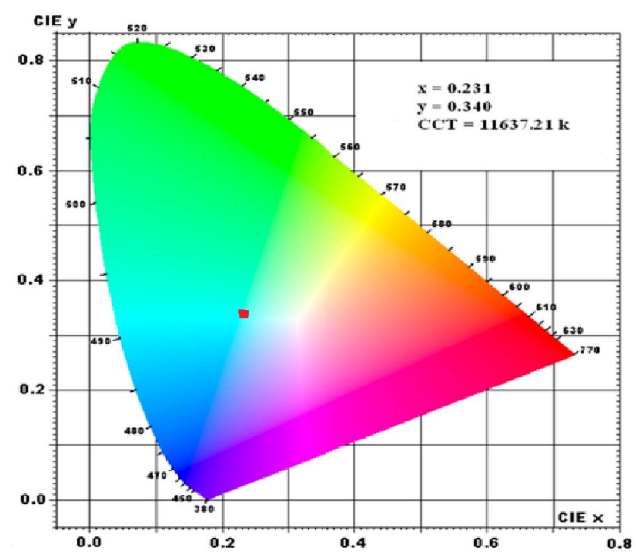

Fig. 13. CIE chromatic diagram of VO^{2+} doped $SrSn(PO_4)_2$ nanopowder.

The bands observed in the FT-IR spectrum indicated the existence of both symmetric and asymmetric stretching and bending modes of phosphate groups. The partial covalent nature of VO^{2+} ions with their ligands was studied by optical

and EPR studies, which further show tetragonal compression for octahedral site symmetry. The emission spectrum showed that cold white light of the prepared sample can be useful for outdoor applications.

ACKNOWLEDGMENTS

Authors are thankful to UGC-DSA (F.No.530/11/DSA-I/2015 (SAP-I)), DST-FIST (F.No.SR/FST/PSI-163/2011(C)), and MHRD-DIC-JNTUK-Satellite center ANU (F.No.4-1/2021-PN-1, dated 30-09-2021) New Delhi for financial assistance to the Dept. of Physics, Acharya Nagarjuna University to carry out the research.

REFERENCES

[1] Sharma, B. K., Wide application feasibility report on graphene. *Emerg. Mater Resear*. **2020**, *9* (4), 1168-1194, https://doi.org/10.1680/jemmr.19.00068.

[2] Dyshlyuk, L.; Babich, O.; Ivanova, S.; Vasilchenco, N.; Atuchin, V.; Korolkov, I.; Russakov, D.; Prosekov, A., Antimicrobial potential of ZnO, TiO_2 and SiO_2 nanoparticles in protecting building materials from biodegradation. *Int. Biodeter. Biodeg.* **2020**, 146, 104821, https://doi.org/10.1016/j.ibiod.2019.104821.

[3] Nirmal Rajeev, Y.; Naveen Kumar, B. V.; Bhushan Kumar, L.; Cole, S., Structural and morphological studies on strontium tin phosphate $SrSn(PO_4)_2$ nanopowder. *Phys. Chem. Resear.* **2022,** *10* (2), 267-271, https://doi.org/10.22036/PCR.2021.300514.1953.

[4] Wang, Z.; Xia, Z.; Molokeev, M. S.; Atuchin, V. V.; Liu, Q., Blue-shift of Eu^{2+} emission in $(Ba,Sr)_3Lu(PO_4)_3$: Eu^{2+} eulytite solid-solution phosphors resulting from release of neighbouring-cation-induced stress. *Dalton. Trans*. **2014**, *43* (44), 16800-16804, https://doi.org/10.1039/C4DT02319F.

[5] Jeevanandam, J.; Sundaramurthy, A.; Sharama, V.; Murugan, C.; Pal, K.; Kodus, M. H. A.; Danquah, M. K., Sustainability of one-dimensional nano-structures: fabrication and industrial applications. *Sust. Nanoscale Eng*. **2020**, 83-113, https://doi.org/10.1016/B978-0-12-814681-1.00004-7.

[6] Abd El-Nasser, S.; Kim, S.; Yoon, H.; Toth, R.; Pal, K.; Bechelany, M., Sodium-assisted TiO_2 nanotube arrays of novel electrodes for photochemical sensing platform. *Org. Elec.* **2020**, *76*, 105443, https://doi.org/10.1016/j.orgel.2019.105443.

[7] Pal, K.; Maria, H. J.; Thomas, S.; Mohan, M. M., Smart in-plane switching of nanowires embedded liquid crystal matrix. *Org. Elec.* **2017**, *42*, 256-268, https://doi.org/10.1016/j.orgel.2016.12.049.

[8] Pal, K.; ed., Hybrid nanocomposites fundamentals, synthesis, and applications. *CRC Press*. **2019**.

[9] Guo, Q.; Liao, L.; Xia, Z., Luminescence properties and energy transfer in $La_6Ba_4(SiO_4)6F_2$:Ce^{3+}, Tb^{3+} phosphors. *Lumin.* **2014**, *145*, 65-70, https://doi.org/10.1016/j.jlumin.2013.07.035.

[10] Rajyalakshmi, T.; Basha, S. J.; Khidhirbrahmendra, V.; Thampy, U. S. U.; Ravikumar, R. V. S. S. N., Synthesis and investigations for white LED material VO^{2+} doped Calcium Cadmium phosphate hydrate nanophosphor. *Molec. Struct*. **2020**, *1205*, 127605, https://doi.org/10.1016/j.molstruc. 2019.127605.

[11] Chander, H., Development of nanophosphors-A review. *Mater. Sci. Eng. R: Rep.* **2005**, *49* (5), 113-155, https://doi.org/10.1016/j.mser.2005.06.001.

[12] West, A. R., Solid state chemistry and its applications. *John Wiley & Sons*, **2022.**

[13] Yu, S.; Xia, Z.; Molokeev, M. S.; Miao, H.; Atuchin, V. V., Synthesis and Luminescence Properties of Blue-Emitting Phosphor $Li_3Sc_2(PO_4)_3$:Eu^{2+}. *ECS J. Solid State Sci. Technol.* **2014**, *3* (8), R159-R163, doi: 10.1149/2.0071408jss.

[14] Khidhirbrahmendra, V.; Basha, S. J.; Avinash, M.; Ravikumar, R. V. S. S. N., Investigations of VO^{2+} doped $SrZn_2(PO_4)_2$ nanophosphors by solution combustion synthesis. *Alloy. Comp.* **2019**, *787*, 276-283, https://doi.org/10.1016/j.jallcom.2019.02.073.

[15] Zhou, H.; Nedley, M.; Bhaduri, S. B., The impacts of Mg^{2+} on strontium phosphate A preliminary study. *Mater. Lett.* **2013**, *113*, 63-66, https://doi.org/10.1016/j.matlet.2013.09.079.

[16] Mal, N. K.; Ichikawa, S.; Fujiwara, M., Synthesis of a novel mesoporous tin phosphate, $SnPO_4$. *Chem. Commu.* **2002**, *2*, 112-113, https://doi.org/10.1039/B109948E.

[17] Rao, K. T. V.; Souzanchi, S.; Yuan, Z.; Ray, M. B.; Xu, C. C., Simple and green route for preparation of tin

phosphate catalysts by solid-state grinding for dehydration of glucose to 5-hydroxy methyl furfural (HMF). *RSC Advan.* **2017**, *7* (76), 48501-48511, https://doi.org/10.1039/C7RA10083C.

[18] Cotton, F. A.; Wilkinson, G.; Murillo, C. A.; Bochmann, M., *Adva. Inorg. Chem.* John Wiley and Sons, Inc, http://repository.vnu.edu.vn/handle/VNU123/85212

[19] Kumar, P. K. K.; Babu, Y. R.; Zyryanov, G. V.; Ravikumar, R. V. S. S. N., Synthesis and spectral characterizations of VO^{2+} ions-doped $CaZn_2(PO_4)_2$ nanophosphor. *SN Appl. Sci.* **2019**, *1*, 1-7, https://doi.org/10.1007/s42452-019-0903-8.

[20] Zhao, D.; Zhang, H.; Xie, Z.; Zhang, W. L.; Yang, S. L.; Cheng, W. D., Syntheses, crystal and electronic structure of compounds $AM(PO_4)_2$ (A = Sr, Ba, M = Ti, Sn). *Dalton Trans*. **2009,** *27*, 5310-5318, https://doi.org/10.1039/B822336J.

[21] Keller, L. P.; McCarthy, G. J.; Grant-in-Aid, I. C. D. D., JCPDS File no. 33-150, North Dakota State University, Fargo, North Dakota, USA, **1982**.

[22] Atuchin, V. V.; Aleksandrovsky, A. S.; Bazarov, B. G.; Bazarova, J. G.; Chimitova, O. D.; Denisenko, Y. G.; Gavrilova, T. A.; Krylov, A. S.; Maximovskiy, E. A.; Molokeev, M. S.; Oreshonkov, A. S., Exploration of structural, vibrational and spectroscopic properties of self-activated orthorhombic double molybdate $RbEu(MoO_4)_2$ with isolated MoO_4 units. *J. Alloys Compd.* **2019**, *785*, 692-697, https://doi.org/10.1016/j.jallcom.2019.01.013.

[23] Alekseev, E. A.; Felbinger, O.; Wu, S.; Malcherek, T.; Depmeier, W.; Modolo, G.; Gesing, T. M.; Krivovichev, S. V.; Suleimanov, E. V.; Gavrilova, T. A.; Pokrovsky, L. D., $K[AsW_2O_9]$, the first member of the arsenate–tungsten bronze family: Synthesis, structure, spectroscopic and non-linear optical properties. *J. Solid State Chem.* **2013**, *204*, 59-63, https://doi.org/10.1016/j.jssc.2013.04.038.

[24] Rebelo, A. H. S.; Ferreira, J. M. F., Comparison of the cadmium removal efficiency by two calcium phosphate powders. *Envi. Chem. Engine.* **2017**, *5* (2), 1475-1483, https://doi.org/10.1016/j.jece. 2017.02.020.

[25] Denisenko, Y. G.; Molokeev, M. S.; Orshonkov, A. S.; Krylov, A. S.; Aleksandrovsky, A. S.; Azarapin, N. O.; Andreev, O. V.; Razumkova, I. A.; Atuchin, V. V., Crystal structure, vibrational, spectroscopic and thermochemical properties of double sulfate crystalline hydrate $[CsEu(H_2O)_3(SO_4)_2]\cdot H_2O$ and its thermal dehydration product $CsEu\ (O_4)_2$. *Crystals.* **2021**, *11* (9), 1027, https://doi.org/10.3390/cryst11091027.

[26] Metwalli, E.; Karabulut, M.; Sidebottom, D. L.; Morsi, M. M.; Brow, R. K., Properties and structure of copper ultraphosphate glasses. *Non-Cryst. Solid.* **2004**, *344* (3), 128-134, https://doi.org/10.1016/j.jnoncrysol.2004.07.058.

[27] Prasad, V. R.; Damodaraiah, S.; Devara, S. N.; Ratnakaram, Y. C., Photoluminescence studies on holmium(III) and praseodymium(III) doped calcium borophosphate (CBP) phosphors. *Molec. Struct.* **2018**, *1160*, 383-392, https://doi.org/10.1016/j.molstruc.2018.02.034.

[28] Krishnan, S. R.; Shanmugam, V. M.; Subramanian, P., EPR and optical studies of VO^{2+} doped potassium succinate-succinic acid single crystal-Substitutional incorporation. *Molec. Struct.* **2017**, *1131*, 149-155, https://doi.org/10.1016/j.molstruc.2016.11.005.

[29] Ramana, C. V.; Carbajal-Franco, G.; Vemuri, R. S.; Troitskaia, I. B.; Gromilov, S. A.; Atuchin, V. V., Optical properties and thermal stability of germanium oxide (GeO_2) nanocrystals with α-quartz structure. *Mater. Sci. Eng. B*. **2010**, *174*, 279-284, https://doi.org/10.1016/j.mseb.2010.03.060.

[30] Abragam, A.; Bleaney, B., Electron paramagnetic resonance of transition ions Clarendon P. **1970**, https://lccn.loc.gov/86006294.

[31] Liu, D.; Lv, Y.; Zhang, M.; Liu, Y.; Zhu, Y.; Zong, R.; Zhu, Y., Defect-related photoluminescence and photocatalytic properties of porous ZnO nanosheets. *Mater. Chem. A*. **2014,** *2* (37), 15377-15388, https://doi.org/10.1039/C4TA02678K.

[32] Lin, J. Z., Theoretical studies of the optical spectra and EPR parameters for VO^{2+} ions in Zn $(antipyrine)_2(NO_3)_2$. *J. Magn. Magn. Mater.* **2013**, 37A4, 453-456.